ORIGINAL PAPER

Water-Weakening and Time-Dependent Deformation of Organic-Rich Chalks

William M. Kibikas[1] · R. Charles Choens[2] · Stephen J. Bauer[1] · Eyal Shalev[3] · Vladimir Lyakhovsky[3]

Abstract

The Ghareb Formation is a shallowly buried porous chalk in southern Israel that is being considered as a host rock for a geologic nuclear waste repository. Setup and operation of a repository will induce significant mechanical, hydrological and chemical perturbations in the Ghareb. Developing a secure repository requires careful characterization of the rock behavior to different loads. To characterize hydromechanical behavior of the Ghareb, several short- and long-term deformation experiments were conducted. Hydrostatic loading tests were conducted both dry and water-saturated, using different setups to measure elastic properties, time-dependent behavior, and permeability. A set of triaxial tests were conducted to measure the elastic properties and rock strength under differential loading at dry and water-saturated conditions. The hydrostatic tests showed the Ghareb began to deform inelastically around 12–15 MPa, a relatively low effective pressure. Long-term permeability measurements demonstrated that permeability declined with increasing effective pressure and was permanently reduced by ~ 1 order of magnitude after unloading pressure. Triaxial tests showed that water saturation significantly degrades the rock properties of the Ghareb, indicating water-weakening is a significant risk during repository operation. Time-dependent deformation is observed during hold periods of both the hydrostatic and triaxial tests, with deformation being primarily visco-plastic. The rate of deformation and permeability loss is strongly controlled by the effective pressure as well. Additionally, during holds of both hydrostatic and triaxial tests, it is observed that when water-saturated, radial strain surpassed axial strain when above effective pressures of 13–20 MPa. Thus, deformation anisotropy may occur in situ during operations even if the stress conditions are hydrostatic when above this pressure range.

Highlights

- Porous chalk was experimentally deformed over short- and long-time scales.
- Water saturation was shown to significantly degrade chalk elasticity and strength.
- Hydrostatic pressure above certain conditions can produce significant deformation anisotropy.
- Chalk samples exhibit strongly visco-plastic and compaction dominated behavior.
- Compaction dominant behavior could inhibit escape of nuclear waste in repository.

✉ William M. Kibikas
  wmkibik@sandia.gov

1 Sandia National Laboratories, Geothermal Department, MS 1033, PO Box 5800, Albuquerque, NM 87185, USA

2 Sandia National Laboratories, Geomechanics Department, MS 1033, PO Box 5800, Albuquerque, NM 87185, USA

3 Geological Survey of Israel, Jerusalem, Israel

1 Introduction

The disposal of nuclear waste remains a critical issue worldwide (Kim et al. 2011; Chapman and Hooper 2012; Ramana 2018). While various solutions have been proposed, there is no established method for isolating nuclear waste over long time scales, leading to many countries pursuing different methodologies (Ali 2011; Faybishenko et al. 2017;

Kuhlman 2017). In Israel, the Israeli Atomic Energy Commission (IAEC) is pursuing use of a borehole repository for disposing of local nuclear waste. In this design, boreholes with diameters upwards of 40 cm would be drilled to the depth of the chosen host formation for waste storage. At the targeted zone, waste would be isolated by both the host rock and engineered barriers, such as cement, bentonite, clays, and backfill (Choens et al. 2021). Given the importance of the host rock in isolating nuclear waste, any potential reservoir must be carefully analyzed to determine its suitability and risk during long-term containment operations. Understanding the host rock behavior over large time scales and how changes to the in situ conditions from operations will affect deformation is the key to demonstrating the viability of a repository and mitigating potential risks of containment failure.

Many countries are considering different rock types for hosting rock types based on their availability and rock properties (Delay et al. 2010; Chapman and Hooper 2012; Cherry et al. 2014). In the USA, salt formations are the primary focus, given their low permeability and ductility (Cherry et al. 2014). Shale and argillite formations are currently being considered in France and Switzerland given their impermeability and plasticity, while granites and other crystalline rocks are under consideration in Russia, China, Finland, and Sweden because of their strength and thermal properties (An et al. 2013; Siren et al. 2015; Laverov et al. 2016). An ideal host rock must be accessible for construction, have low permeability, and be able to avoid fracture formation due to in situ changes generated by the repository construction and operation.

Porous sedimentary rocks are of particular significance, given their ubiquity in the shallow crust (0–10 km). Because of their accessibility and ability to contain fluids, they are relevant to many engineering applications, including hydrocarbon extraction, waste fluid disposal, and CO_2 sequestration. As such, porous rock deformation behavior has been extensively studied experimentally (Wong and Baud 1999; Klein et al. 2001; Wong et al. 2001; Fortin et al. 2009; Brantut et al. 2014; McBeck et al. 2022) and in the field (Teufel et al. 1991; Schutjens et al. 2004; Agosta et al. 2010). The deformation of chalk, a fine-grained porous carbonate, has been of particular interest due to chalk importance in hydrocarbon recovery (i.e., Teufel et al. 1991; Amour et al. 2021) and quantifiable observations of water-weakening in reservoirs (Ruddy et al. 1989; Risnes et al. 2005; Kallesten et al. 2021). However, the properties of chalk and many other porous rocks, aside from shales, relevant to deformation during nuclear waste disposal operations remain largely uncharacterized.

Several coupled mechanical and hydrological considerations must be accounted for during repository selection. First, the borehole must be stable during operation and unlikely to deform in a way that risks environmental leakage (Brady et al. 2009, 2012). This is primarily determined by the in situ stress conditions and the mechanical properties of the host rock (Beswick et al. 2014). Excavation and operation of the repository are likely to impose additional loading to the surrounding rock, and the formation's mechanical properties will control whether deformation around the borehole occurs as fracturing or plastic flow. The hydrologic behavior during operations is much more difficult to discern. In a low permeability rock, fractures act as the primary path for fluid flow. Fracture strength can be predicted with an understanding of the local mechanical properties, but the stress-dependent permeability of existing fractures is difficult to constrain because they are very sensitive to localized changes in fracture properties and heterogeneity (Rutqvist 2014). Predicting the host rock permeability under different mechanical loads requires a very careful calibration of the coupled hydromechanical behavior in the host rock (Tsang et al. 2012). Additionally, containment of nuclear waste must maintain isolation over large time scales (> 1000 years), though containment on short and intermediate time scales (< 1000 years) is also important as the rate of deformation in the host rock tends to decay with time (Sasaki and Rutqvist 2022). These time scales require significant modeling of the hydromechanical behavior of the host rock, especially in the near borehole zone, which require understanding of the repository behavior in order to accurately determine and mitigate the risk of nuclear waste leakage.

The IAEC is currently considering the Ghareb Formation, a shallow porous chalk horizon in southern Israel, as potential host rock. However, the hydrological and mechanical behavior of the formation is not well understood, especially the time-dependency of its deformation over large time scales. In order to accurately model the behavior of the repository and determine formation suitability as a host rock, several sets of experimental tests were conducted on samples of the Ghareb. The hydrological and mechanical properties were determined from short (e.g., 1 h) to long (e.g., 100 days) time scales. The different sets of experiments are used to show how the deformation processes are strongly coupled in the Ghareb, and that minute changes to any condition can dramatically alter the long-term stability of the rock during repository operation. This work provides much needed understanding of the long-term behavior of the Ghareb which previous studies involving this formation have not attempted to quantify.

2 Materials, Sample Preparation, and Procedures

2.1 Ghareb Formation and Sample Preparation

The Ghareb Formation is an Upper Cretaceous organic-rich chalk in the Mt. Scopus Group in Israel, primarily composed

primarily of fine-grained carbonate and clay grains (Bisnovat et al. 2015; Shitrit et al. 2016, 2017). Table 1 shows XRD data for identified minerals phases in Ghareb samples from previous studies to show mineralogy (Shitrit et al. 2017; Dangelmayr et al. 2022; Jove-Colon et al. 2022).

The formation has massive bedding, high porosity (20–45%), high kerogen content, and high sulfur content (Koopmans et al. 1998; Shitrit et al. 2016). The formation permeability is low, ranging from 10^{-15} to 10^{-18} m^2 (Bisnovat et al. 2015). Formation thickness is highly variable, but Ghareb thickness in our area of study can be as much as 200–400 m (Fig. 1) (Shitrit et al. 2016).

Host rock material was collected as blocks from a surface quarry (Fig. 1—ellipse). Microscopic analysis of our rocks was conducted using scanning electron microscope (SEM) images (Fig. 2). The quarried rock has a matrix of clay-sized particles with micro- to macro-fossils (calcite), clastic grains (quartz, feldspar), and lithic clasts (igneous and sedimentary rocks) throughout. There is a small but detectable preferred orientation of the very fine-grained clay lenses, some elongate grains, and lenses of closely spaced silicate grains. Very little matrix or intergranular porosity is present. A few pores defined by thin-walled fossils appeared to be slightly crushed in alignment with preferred orientation of matrix

Table 1 Weight percent (wt%) values calculated from XRD modal analysis of core sections of the Ghareb Formation

Mineral	Dangelmayr et al. 2022, CK-6 Weight percent (%)	Dangelmayr et al. 2022, OS-3 Weight percent (%)	Jove-Colon et al. 2022 Weight percent (%)	Shitrit et al. 2017 Weight percent (%)
Calcite	83.20	44.60	95.49	59.74
Dolomite	0.60	3.30	–	1.02
Quartz	0.70	2.70	0.96	3.79
Apatite	–	7.60	–	23.06
Potassium Feldspar	–	10.50	–	0.92
Plagioclase Feldspar	–	13.70	-	0.97
Pyrite	–	–	–	1.81
Halite	–	–	0.40	–
Sylvite	–	–	0.37	–
Clay Fraction*	14.70	17.10	2.78	8.29
Organics	0.11	11.0	–	0.40

*The primary clay minerals observed were smectite, illite, and kaolinite, with smectite being the dominant clay observed

Fig. 1 Surface map of lower Israel showing previous areas of study, with the potential repository enclosed within the ellipse
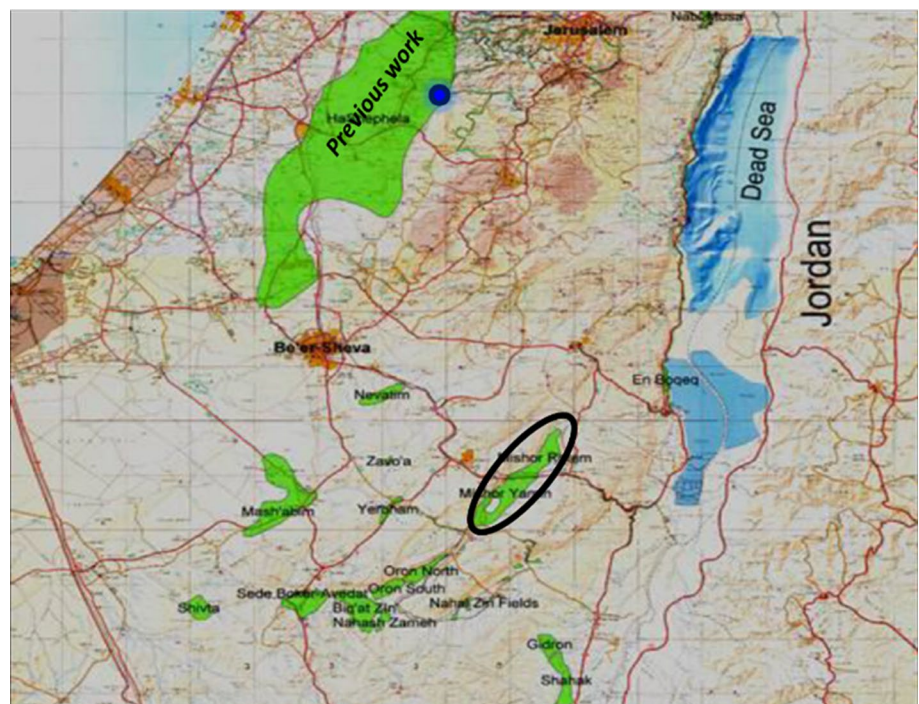
and grains, suggesting partial diagenetic-related compaction of the Ghareb.

As the bulk formation is massive, our material lacked significant bedding or obvious layering once quarried. Cored cylindrical samples were prepared into right cylinders for experimental testing according to ASTM standard (ASTM 2001) (Fig. 3a, b). Each sample was oven-dried at 40 ˚C for over 24 h before dimensions and weights were recorded prior to testing. Initial saturation was not determined as these were quarried materials.

2.2 Hydrostatic Loading and Creep-Permeability Tests

Samples were placed between two steel platens and coated with an ultraviolet light-cured polyurethane (Fig. 3d) prior to testing. Two axial and two lateral LVDTs (Linear Variable Displacement Transducers) were attached to the endcaps and across the sample diameter to measure sample deformation. The axial and lateral transducers are used to determine the axial and radial strain (ϵ_{ax} and ϵ_{rad} respectively) during testing, while volumetric strain (ϵ_v) is determined through:

$$\varepsilon_v = \varepsilon_{ax} + (2 * \varepsilon_{rad}) \tag{1}$$

The typical rock mechanics convention is used here where positive stress/strain indicates compaction while negative stress/strain indicates tension. All water-saturated tests were pre-dried and saturated in the pressure vessel by adding a small confining pressure and applying a differential pore pressure for > 1 h to flow water through each sample and ensure saturation.

Three types of hydrostatic loading tests were conducted. The first and second types were conducted using a
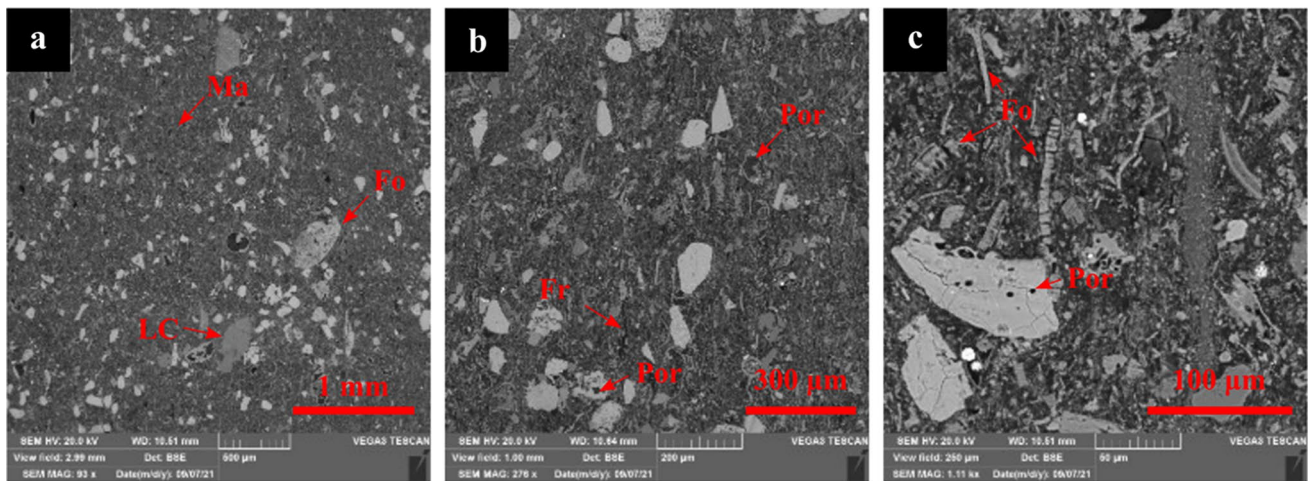

Fig. 2 SEM images of undeformed Ghareb material used in experimental tests. **a** Dominantly a fine-grained matrix composed of calcite fossils (Fo), with a small number larger lithic clasts (LC) and grains scattered throughout. **b** A small number of pores (Por) exist in fossil grains and where grain collapse has occurred; subparallel fracturing (Fr) does appear to exist following a possible preferred orientation of the grains. **c** Matrix is a composite of fossil fragments scattered around larger grains; elongate grains in the matrix do seem to possess a slight preferred orientation, though this is not visible with more rounded grains

Fig. 3 Examples of tested cylinders shown in **a**, **b** and **c**, while d shows general setup of samples during deformation tests
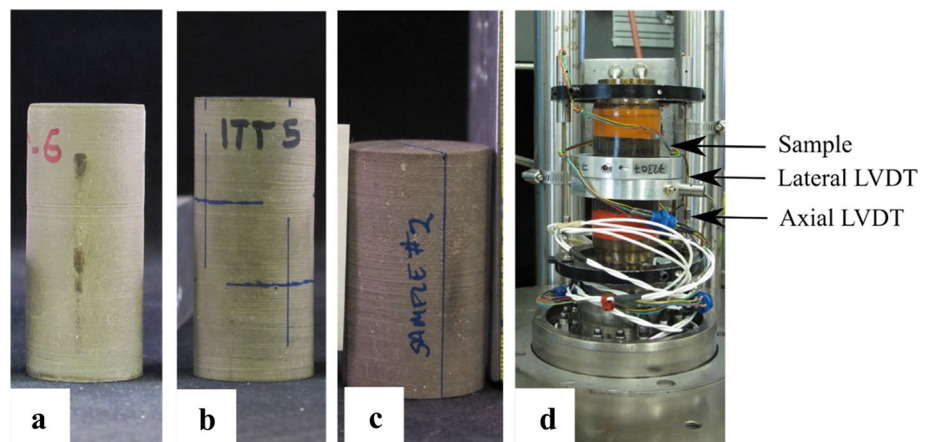
servo-hydraulic loading frame (978 kN) and external pressure vessel in Fig. 4a, while the third type was conducted using the customized pressure system shown in Fig. 4b. Hydrostatic loading paths are shown in Fig. 5.

In the first test type (Fig. 5a, HL1), confining pressure (σ_c) was increased at a constant rate during testing (~3 MPa/min). Once the intervals of 25, 50, 75, 100, 130, 160, 200, 300, and 400 MPa were reached, the confining pressure loading was halted and then reduced at the same rate. Once unloaded to 60–70% of the interval pressure (e.g., 25, 50, 75, etc.), unloading was stopped and confining pressure was increased to the next interval. These unload–reload loops were performed to measure stress and strain for calculating the bulk modulus (K) of the sample with increased confining pressure, using the formula:

$$K = \frac{\sigma_{eff}}{\varepsilon_v} \tag{2}$$

where σ_{eff} and ϵ_v are the effective confining pressure and volumetric strain, respectively. σ_{eff} was calculated as the difference between σ_c and the pore pressure (σ_p). Once confining pressure was increased to 400 MPa, and the unload-reload loop was conducted, confining pressure was unloaded and the test concluded. For this first type of test, the sample was deformed dry with no pore pressure. The extremely high confining pressure applied during the test (400 MPa) allowed for full characterization of how the inelastic (i.e., non-recoverable) behavior of the Ghareb changed with increasing deformation and pore closure.
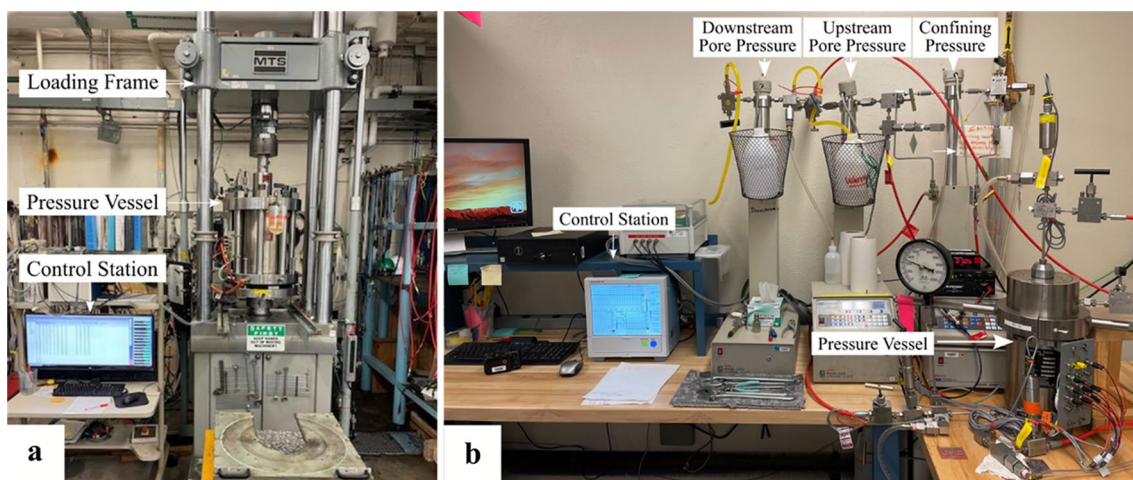

Fig. 4 **a** 978 kN load frame and 100 MPa pressure vessel used for high pressure hydrostatic and triaxial tests; **b** 69 MPa pressure vessel and fluid system for long term hydrostatic creep tests
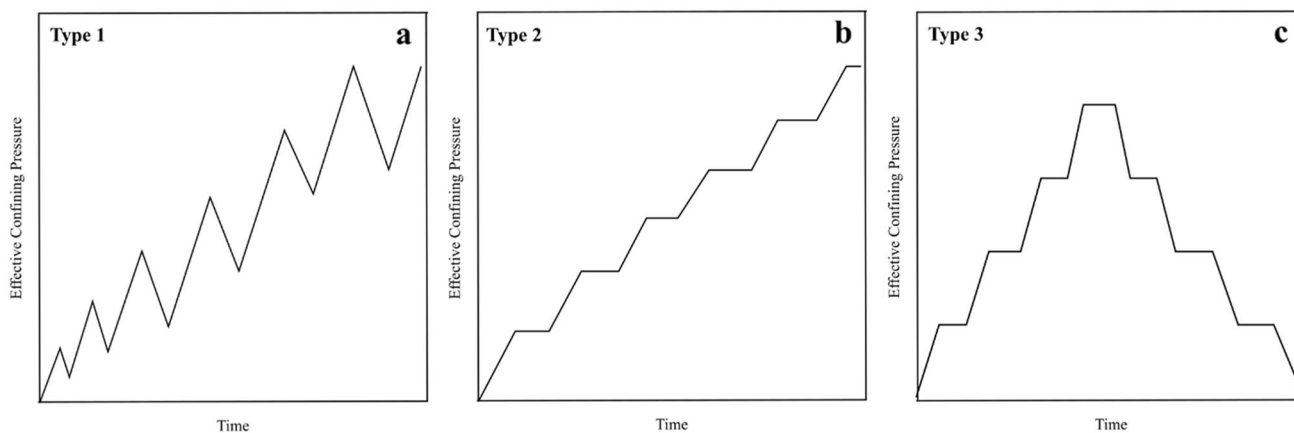

Fig. 5 Schematics of the three hydrostatic loading paths: **a** test type 1—hydrostatic loading with unload-reload loops; **b** test type 2—hydrostatic loading with pressure holds for creep testing; **c** test type 3—long-term hydrostatic creep tests with permeability measurements. The scale for Type 1 and 2 is different than Type 3, which experienced only 20.8 MPa effective pressure at the maximum and was conducted over a period of three months

For the second test type (Fig. 5b), dry and wet samples (HC1 and HC2 respectively) were confined and tested in a similar manner to the first test, using a similar pressure loading rate (~ 3 MPa/min). Instead of unloading pressure at intervals though, the confining pressure was held constant for a period of 1–2 days at each interval to measure creep strain. Confining pressures during each test were held at 25, 50, 100, 150, 200, 250, 300, 350 and 400 MPa. For HC2, σ_p was increased to 5 MPa at the first loading interval and held constant throughout the test. Confining pressure was increased in intervals up to 400 MPa for both tests and then unloaded.

The third type of hydrostatic test involved measuring the long-term creep strain and permeability of three samples under hydrostatic conditions (Fig. 5c). Confining pressure and pore pressure were applied with three external syringe pumps (one for confining pressure, one for upstream pore pressure, and one for downstream pore pressure). Samples were jacketed with LVDTs similar to the triaxial tests (Fig. 3d), then placed into a pressure vessel (Fig. 4b). Confining pressure was then increased to 1–2 MPa and pore pressure both upstream and downstream to ~ 0.69 MPa. The samples were held at these conditions to saturate for 2–3 days. Then confining pressure was increased stepwise (loading rate of 0.3–0.4 MPa/min) while upstream and downstream pressure varied to produce a pore pressure differential (i.e., upstream pore pressure was ~ 0.7 MPa greater than the downstream pore pressure). Confining pressure intervals for holding at all tests were approximately 2.07, 4.14, 6.90, 10.34, 13.79, 20.68, 17.24, 13.79, 6.90, 3.45, 2.41, and 1.38 MPa. At each pressure step, conditions were maintained for several days to observe the creep and permeability (Eq. (3)), and once stable, pressure was increased to the next stage. Confining pressure was increased up to 20.7 MPa, held for 2–5 days, then pressure was decreased in a similar stepwise manner. Tests were conducted for a period of 70–100 days.

The apparent permeability (k) during all tests was determined using a modified version of Darcy's law in the form of:

$$k = \frac{2 * L * \mu * Q * \left(P_{dn}\right)}{A * \left(P_{up}^2 - P_{dn}^2\right)} \tag{3}$$

where L and A are the sample length and flow cross-sectional area, respectively, P_{up} and P_{dn} are the upstream and downstream pore pressures, μ is the dynamic fluid viscosity (e.g., water = 1.0016 mPa*s and air = 0.01813 mPa*s), and Q is the volumetric fluid flow rate. No Klinkenberg correction was performed for the gas permeability calculations (e.g., Klinkenberg 1941).

2.3 Triaxial Deformation Tests

The triaxial deformation tests were conducted using the same loading frame as the first two hydrostatic tests (Fig. 4a). All samples were loaded hydrostatically at a constant rate to a predetermined confining pressure and pore pressure (Table 2). Then each sample was axially loaded with a constant axial strain rate of 10^{-5} s^{-1}. Unload–reload loops were performed during axial loading to measure the elastic moduli at various stages of deformation.

Two types of triaxial test procedures were used (Table 2). For the first type (TP1–TP3), dry samples were initially loaded to ~ 3.5 MPa confining pressure. Then a pore pressure was applied using gas (nitrogen) at one end of the sample with the other end of the sample open to the atmosphere. This created a pore pressure differential that allowed for the measurement of permeability. Samples were then allowed to sit for 1–2 days before being raised to the final confining pressure. This hold at hydrostatic conditions before differential stress was applied is referred to here as "pre-axial holds," during which permeability and strain were recorded (Fig. 6a). Permeability during the holds was measured using air as a permeant and permeability was calculated with Eq. (3). Samples were then deformed axially, with a constant axial strain rate of 10^{-5} s^{-1} up to as much as 9% axial strain. 2–5 unload–reload loops (Fig. 6a) were conducted per test to measure elastic properties, to minimize inelastic (i.e., non-recoverable) deformation being included in the elastic moduli calculations. During the unload–reload loops, the differential stress was unloaded to 0 MPa and held constant for ~ 1 h. These holds after unloading differential stress to 0 are referred to as "mid-axial holds", recording the permeability and strain to show the evolution in behavior with each subsequent application of differential stress (Fig. 6b). After 1 h, differential stress was reloaded and increased to a new value before unloading again (Fig. 6a). After the mid-axial holds and unload–reload were completed, samples were axially loaded at a constant rate until failure or consistent mechanical behavior was observed. Once axial loading was complete, differential stress was decreased to 0 MPa and samples were held under confining pressure for ~ 12–18 h. These holds after differential stress testing was completed are referred to here as "post-axial holds" or "post-axial loading."

Samples TP4 and TP5 employed the same load path, but samples were water-saturated with similar pore pressures using water rather than nitrogen. Although the procedure was largely the same, both upstream and downstream pore pressures were constant at 0.69 MPa, so permeability could not be determined (see Table 2).

Table 2 Conditions for testing of all hydrostatic and triaxial deformation tests

Test Name	Loading Path	Length mm	Diameter mm	Weight g	Density g/cm^3	Condition Wet/Dry	P_c MPa	P_p MPa	Permeability
HL1	H	53.26	37.90	93.33	1.55	Dry	0–400	–	No
HC1	HC	85.47	37.29	131.38	1.41	Dry	0–400	–	No
HC2	HC	81.97	37.90	142.68	1.54	Wet	0–400	5	No
HP1	HCP	40.72	24.56	27.56	1.43*	Wet	0–20.7	0.3–1.7	Yes
HP2	HCP	40.72	24.59	29.29	1.51*	Wet	0–20.7	0.3–1.7	Yes
HP3	HCP	36.04	24.59	24.29	1.42*	Wet	0–20.7	0.3–1.7	Yes
TP1	TCP	77.44	37.74	122.65	1.41	Dry	20.7	0.6	Yes
TP2	TCP	81.59	37.59	136.05	1.50	Dry	3.5	0.6	Yes
TP3	TCP	88.52	37.64	144.16	1.46	Dry	6.9	0.6	Yes
TP4	TC	85.37	37.64	134.44	1.41	Wet	3.5	0.6	No
TP5	TC	66.45	37.62	102.75	1.39	Wet	20.7	0.6	No

Loading paths: *H* hydrostatic, *C* creep, *T* triaxial, *P* permeability

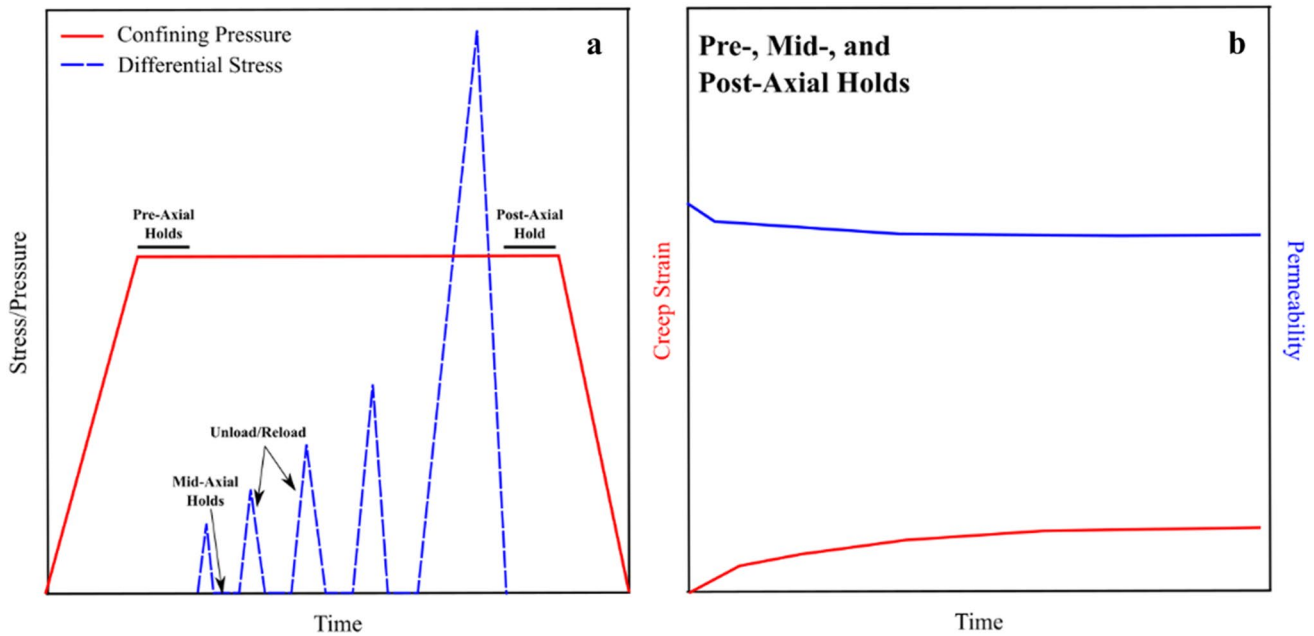*Density was calculated from the water-saturated samples only

Fig. 6 Schematic for triaxial tests showing the differential stress loading path (**a**) and measurements during each hold at 0 MPa differential (**b**)

Elastic moduli were calculated from the unloading portion of the unload-reload loops during triaxial tests. Young's modulus (*E*), Poisson's ratio (*ν*), and shear modulus (*G*) were calculated from the stress and strain data using:

$$E = \frac{\sigma_{ds}}{\varepsilon_{ax}} \qquad (4)$$

$$v = -\frac{\varepsilon_{rad}}{\varepsilon_{ax}} \qquad (5)$$

$$G = \frac{\tau}{\gamma} \qquad (6)$$

where σ_{ds}, τ, and γ are the differential stress, shear stress, and shear strain, respectively. To determine shear stress and strain during axial loading, the convention is adopted that shear stress in this setup is equivalent to $(\sqrt{(1/3)}*\sigma_{ds})$, while shear strain is treated as the second invariant of the deviatoric strain tensor (Rudnicki 2004).

3 Experimental Results and Discussion

3.1 Hydrostatic Loading, Creep, and Permeability

3.1.1 Hydrostatic Loading Tests

Mechanical data for the hydrostatic loading tests up to a confining pressure of 400 MPa are shown in Fig. 7 with effective pressure plotted against volumetric strain. Sample behavior of the hydrostatic loading can be described with several stages: (1) an initial "toe" portion of nonlinear compaction (0–2 MPa), (2) a period of quasi-linear strain (2–12 MPa) where deformation is primarily elastic, (3) a transition to nonlinear compaction where increasing stress generates greater compaction than previously (12–100 MPa), but with increasing stress the change in volumetric strain decreases (100–400 MPa). Similar behavior has been exhibited in other porous rocks, such as sandstone (Zhang et al. 1990; Fortin et al. 2009) and limestone (Vajdova et al. 2004; Brantut et al. 2018) and can be attributed to: (1) closing of existing cracks and grain re-arrangement, (2) elastic compression of the grain and pore structure, (3) inelastic deformation mechanisms, such as grain crushing and pore collapse (Zhang et al. 1990; David et al. 2001). The transition between elastic and inelastic deformation referred to as the $P*$ or grain crushing pressure occurs where loading behavior transitions from Stage 2 to Stage 3 (Fig. 5a). The $P*$ values identified for HL1 (12.5 MPa), HC1 (13.4 MPa), and HC2 (13.0 MPa),
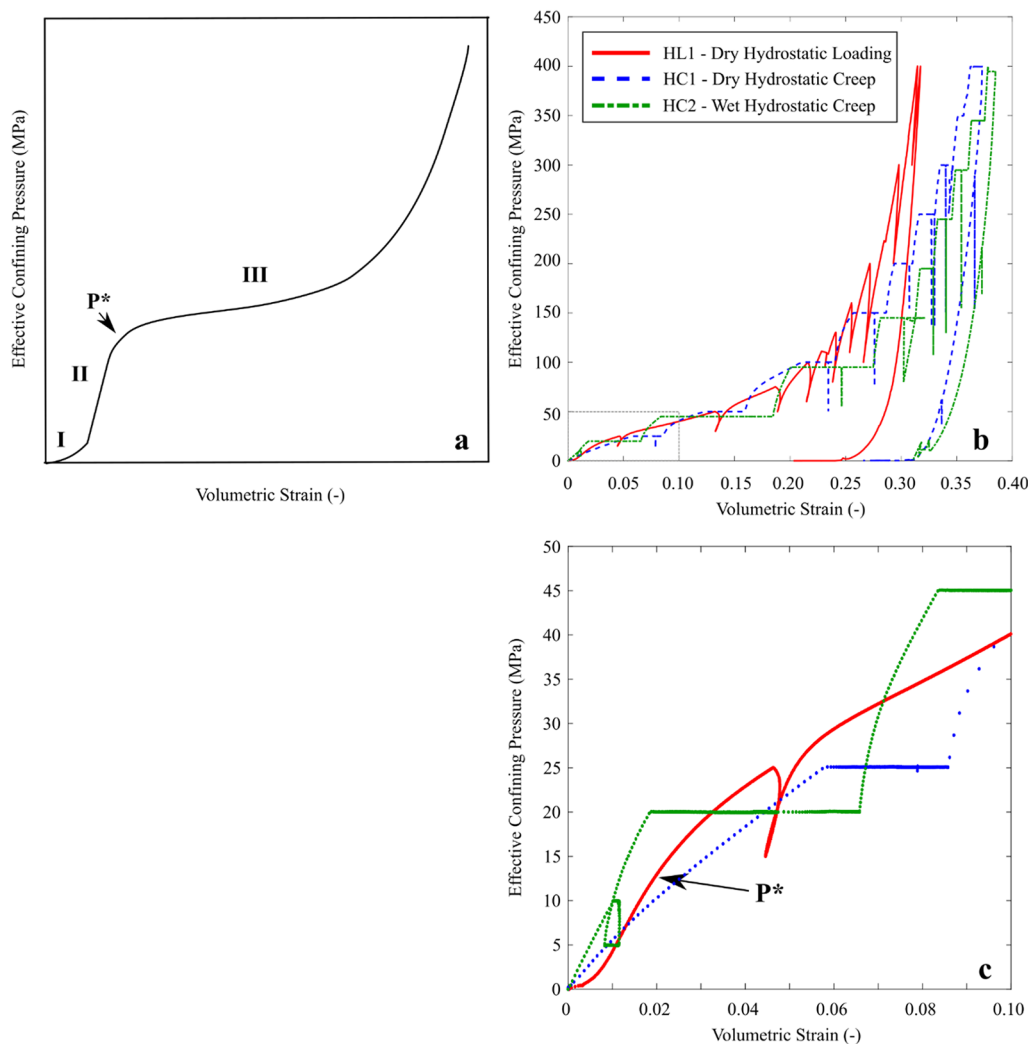

Fig. 7 A schematic of hydrostatic compaction stages is shown in (**a**), complete hydrostats up to 400 MPa are shown in **b** and **c** shows the zoomed in area of the gray box in (**b**), highlighting the transitions from stages 1, 2, and 3 as well as $P*$. The dry hydrostatic loading test (HL1) up to 400 MPa confining pressure is shown alongside the dry and water-saturated hydrostatic creep tests (HC1 and HC2 respectively) up to 400 MPa confining pressures

suggest the transition from elastic to inelastic deformation occurs from 12 to 14 MPa (Fig. 7c). Given the relatively low transition to inelastic behavior for the hydrostatic tests, it can be assumed that most of the deformation of the samples was through inelastic strain, especially given the fairly high volumetric strain exhibited after pressure was unloaded to 0 MPa (e.g., $\epsilon_v = 0.2-0.3$).

The behavior of the creep tests (HC1 and HC2) is different from the constant loading test (HL1). First, higher amounts of strain are exhibited during loading by both creep tests due to longer loading periods. The dry and water-saturated tests are not identical; the water-saturated test exhibits greater strain (~0.01–0.05) for a given stress, especially during the hold periods. The amount of strain occurring during creep appears to diminish as confining pressure is increased, such that at higher pressures the difference between the dry and water-saturated tests appears negligible. The fact that the permanent strain after unloading pressure from both creep tests is nearly the same supports this diminishing effect of higher pressures.

3.1.2 Hydrostatic Creep-Permeability Tests

The long-term hydrostatic creep test data, including stresses, strains, and permeability, is shown in Fig. 6. All three samples showed increasing strain with each increase in confining pressure and pore pressure. When pressure was held constant, strain continued to accumulate over time characteristic of creep or time-dependent behavior, with greater strain rates at greater pressures. The largest increase in strain and strain rate occurs when pressure is increased from 13.7 to 20.7 MPa such that the volumetric strain more than doubles during the first few hours after pressure was increased. It is also at this pressure condition that radial strain accumulated surpasses axial strain, despite the hydrostatic conditions. It also noteworthy that HP1 exhibits nearly identical strain accumulated to HP2 and HP3 when loaded up to 13.7 MPa, but after which HP2 and HP3 exhibited 0.01–0.02 more strain for the remainder of the test. This may also be related to that HP1 exhibits much lower permeability throughout the test, while HP2 and HP3 exhibit 1–2 orders of magnitude higher permeability (HP2 and HP3 permeability values are similar to one another as well). After each decrease in pressure, strain continued to decrease while confining pressure was held constant, with greater strain reduction over time at each lower pressure step. For all tests and holding conditions, each test exhibited first and secondary creep, but not tertiary creep (creep failure) (e.g., Brantut et al. 2013). When pressure was reduced to 0 MPa, all tests exhibited 0.04–0.05 inelastic, or non-recoverable, volumetric strain (Fig. 8b, e, h).

Permeability of each test is shown to decrease dramatically as effective pressure is raised above ~2 MPa, though the reduction in permeability occurs at the lowest confining pressure increase. However, as effective pressure was decreased, permeability did not concurrently return to its original values, remaining 0.5 to 1.5 orders of magnitude lower than the initial values measured at the test start. Behavior during unloading differed between each test, either continuing to decrease until the lowest effective pressures (HP1, Fig. 8c), remaining fairly constant until effective pressure was decreased below ~10 MPa then increasing moderately (HP2, blue line in Fig. 8f), or remaining constant until effective pressure was decreased below ~10 MPa then increasing slightly (e.g., increase only 2.5× from lowest permeability) (HP3, green line in Fig. 8i).

The difference between the observed permeability measurements may be related to the strain measurements mentioned previously. It should be noted that the axial strains of the three tests are similar at a given pressure condition, while the radial strain of HP2 and HP3 are nearly twice the value in HP1 after reaching 20.68 MPa confining pressure. This difference in the deformation of each sample may contribute to the variance in permeability change as pressure is unloaded in the tests (Eq. (3)), as greater reduction of the length or area during testing could decrease or increase permeability, respectively.

3.2 Triaxial Tests and Creep

3.2.1 Dry and Wet Experiments

Experimental results for both dry and water-saturated tests are shown in Fig. 9, comparing the axial, radial (Fig. 9a), and volumetric (Fig. 9b) strains against differential stress. Porous rocks undergoing axial deformation typically transition through several stages of deformation with increasing stress: (1) linear–elastic deformation where stress–strain behavior does not deviate from the hydrostat; (2) a transition point or yield stress where deformation becomes nonlinear and mechanisms such as micro-cracking dominate; (3) deformation localizes and forms a macroscopic fracture that greatly decreases load bearing capability. (1) and (2) can be seen occurring in all samples tested in Fig. 9, though (3) is only observed for the tests at 2.9 MPa.

For the tests shown in Fig. 9, a few points are immediately clear. The rocks are not very brittle, as the only sample that exhibits a stress drop indicative of shear localization and failure is the dry test at 2.9 MPa (Fig. 9a). All other tests exhibit work hardening during loading. Looking at the volumetric strains in Fig. 9b, the volumetric strain initially is consistent for all tests, but with increased loading the slope of volumetric strain decreases, indicating deformation is compaction dominant. As differential stress increases, the tests at 2.9 MPa eventually transition from compaction dominant behavior (positive volumetric strain slope)
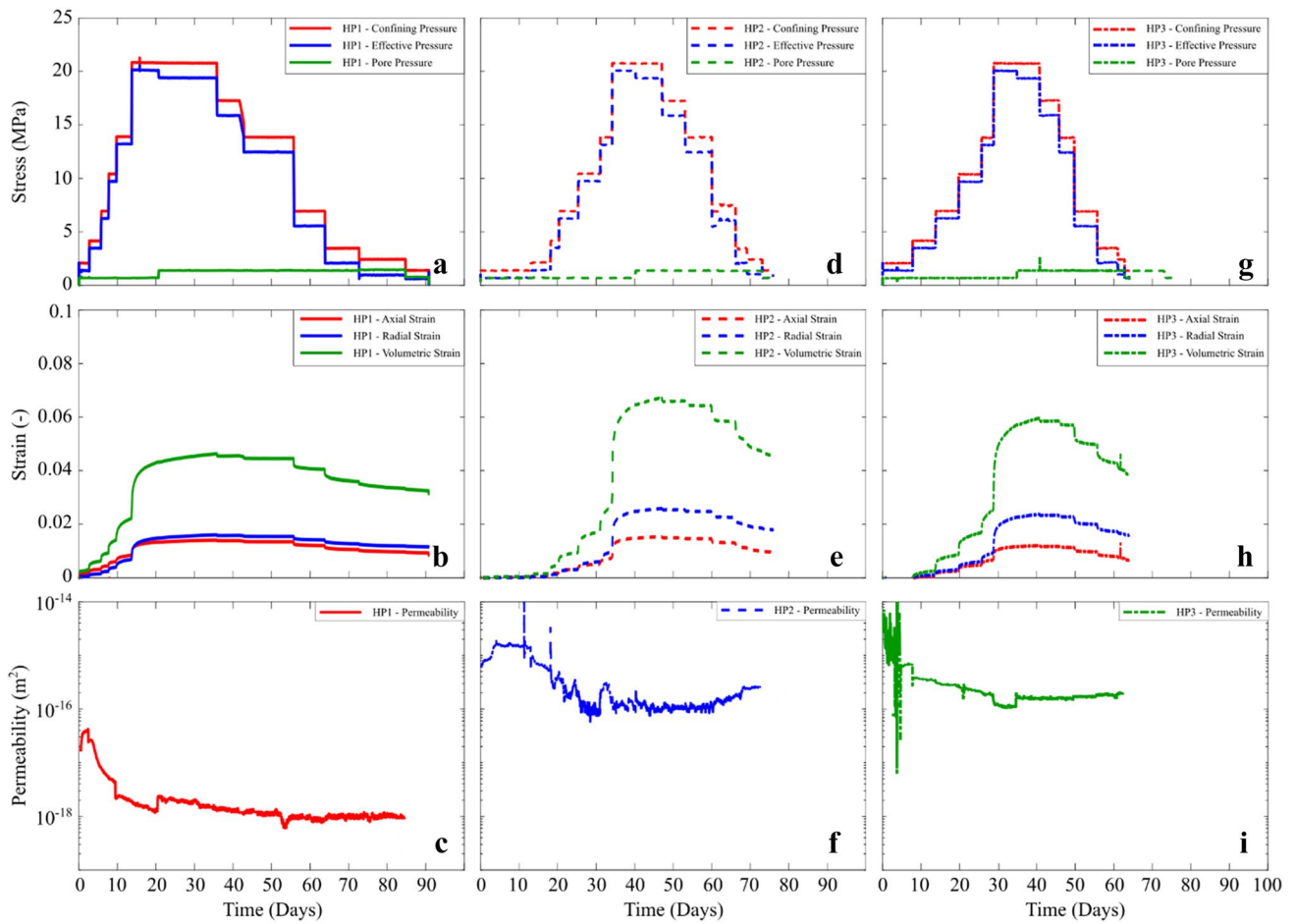
Fig. 8 Hydrostatic long-term creep test data showing time against stress, strain and permeability for HP1 (**a**, **b**, **c**), HP2 (**d**, **e**, **f**), and HP3 (**g**, **h**, **i**) Top row shows pressures, center row shows strains, bottom row shows permeability
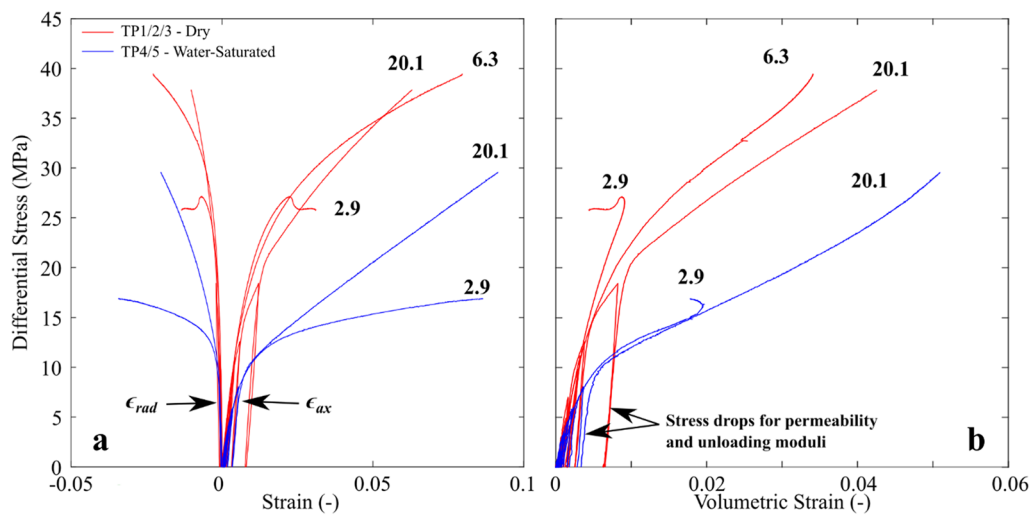

Fig. 9 Differential loading of dry (red) and water-saturated (blue) tests under effective pressure indicated next to each curve: **a** axial (ϵ_{ax}) and radial (ϵ_{rad}) strain; **b** volumetric strain (ϵ_v). The stress drops observed occur during each test to measure both the unloading moduli and the permeability at 0 MPa

to dilation dominant behavior (negative volumetric strain slope). The tests at 6.3 and 20.1 MPa (TP5 only) primarily exhibit shear-enhanced compaction, though they do seem to be slowly showing more dilation behavior with increased strain (Fig. 9b). These results are consistent with observations that the stress required for dilation dominant behavior to occur increases with effective pressure. This transition indicates that micro-mechanisms such as fracturing become the dominant mechanism of deformation.

Comparing the dry and water-saturated tests, water noticeably affects deformation at the same conditions. Water saturation appears to reduce rock strength, as both the 2.9 and 20.1 MPa tests become inelastic at lower differential stresses, exhibit 10–20 MPa lower strength for a given axial strain, and exhibit more compaction dominant behavior than the dry tests at the same conditions.

3.2.2 Pre-, Mid-, and Post-Axial Loading Holds

Gas permeability and volumetric strain measurements at each hydrostatic and differential loading hold are shown in Fig. 10. Only the dry tests TP1, TP2, and TP3 have permeability data (Table 2), but the creep strain data during each hold is shown for all tests.

Comparing permeability measurements during each hold period, values are shown to decrease with increasing effective pressure during the hold periods (Fig. 10a, b). For example, the lowest pre- and post-axial loading permeabilities (Fig. 10b) are exhibited by TP1 at 20.1 MPa and the greatest are exhibited by TP2 at 2.9 MPa effective pressure. Further, the role of effective pressure can be seen in Fig. 8a, as the reduction of permeability between loading cycles when the effective pressure is lower, hence the large variance measured during TP2 but less during TP1.

The volumetric strains in Fig. 10c and d show how strain evolved between each holding period. As the axial loading holds primarily occurred in the elastic region of deformation, variation between axial loads was not large. However, it is noteworthy that the values measured for TP1 and TP5, with effective pressures of 20.1 MPa, show more variance between each cycle than is observed for the lower pressure tests. Such an observation could be related to effective pressure introducing greater inelastic deformation at lower stresses.

4 Analysis and Discussion

4.1 Mechanical Properties and the Impact of Rock-Fluid Interaction

Rock behavior is often quantified through a set of mechanical properties, such as the elastic moduli and stress points.

These values are used to model how rocks will behave in situ under various conditions that cannot be easily or safely tested in the field. Thus, to understand how the Ghareb will behave over time, it is necessary to characterize these various properties.

Elastic moduli are shown in Table 3, calculated using Eq. (4–6). The bulk moduli measured during hydrostatic loading/creep experiments were measured at multiple effective pressures and are compared in Fig. 11. The highest K values are observed in HL1, where conditions were dry, and stress was not held constant to allow for creep. The moduli measured for HL1 were comparable to those observed by Bisnovat et al. (2015) for hydrostatic compression of dry Ghareb rocks, who found that irreversible compaction occurred around 20 MPa. Interestingly, HC2 (wet) had higher K values than the HC1 test (dry) despite the effect of water. In general, K increases with effective pressure since greater pressure closes pore spaces and deformation of the rock skeleton becomes dominant with increased compaction (David et al. 1994; Bernabé et al. 2003). The lower K for the HC1 compared to HL1 and HC2 may be a result of the porosity of the samples. Both HL1 and HC2 have initial porosities of ~0.27, whereas HC1 had an initial porosity of ~0.34. The initial porosity thus seems to be the main control on the value of K for a given pressure in the Ghareb rocks under hydrostatic loading conditions (e.g., Shitrit et al. 2016).

The triaxial deformation tests allow for the determination of E, ν, and G. The mean values for all the unloading measurements during each test were found and plotted in Fig. 12. To show variance, bars are plotted showing ± 1 standard deviation (Table 3).

Values of E either remain constant with increasing effective pressure (dry) or increase slightly with effective pressure (water-saturated). Conversely, the slopes of G and effective pressure are much less than observed E values. ν measured for both the dry and water-saturated tests are more consistent as both increase concomitantly with effective pressure (Fig. 12c). Comparing the dry and water-saturated properties quantified, the effect of rock-fluid interaction can be shown. Both E and G are greater for the dry tests than for the water-saturated tests, while ν for both dry and water-saturated tests are close, with slightly higher values observed under water-saturated conditions. Generally, higher values of E and G, and lower values of ν, are observed in rocks with lower porosity, greater density, greater rock strength, and lower shear angles (Martin 1997). Given the limited number of tests for both dry and water-saturated conditions, it is possible the fits shown are in fact non-linear, particularly at very low (< 1 MPa) or very high (> 100 MPa) effective confining pressures. However, the Ghareb in situ is unlikely to experience such extreme pressure conditions given its shallow burial, even during operation of a geologic waste repository.
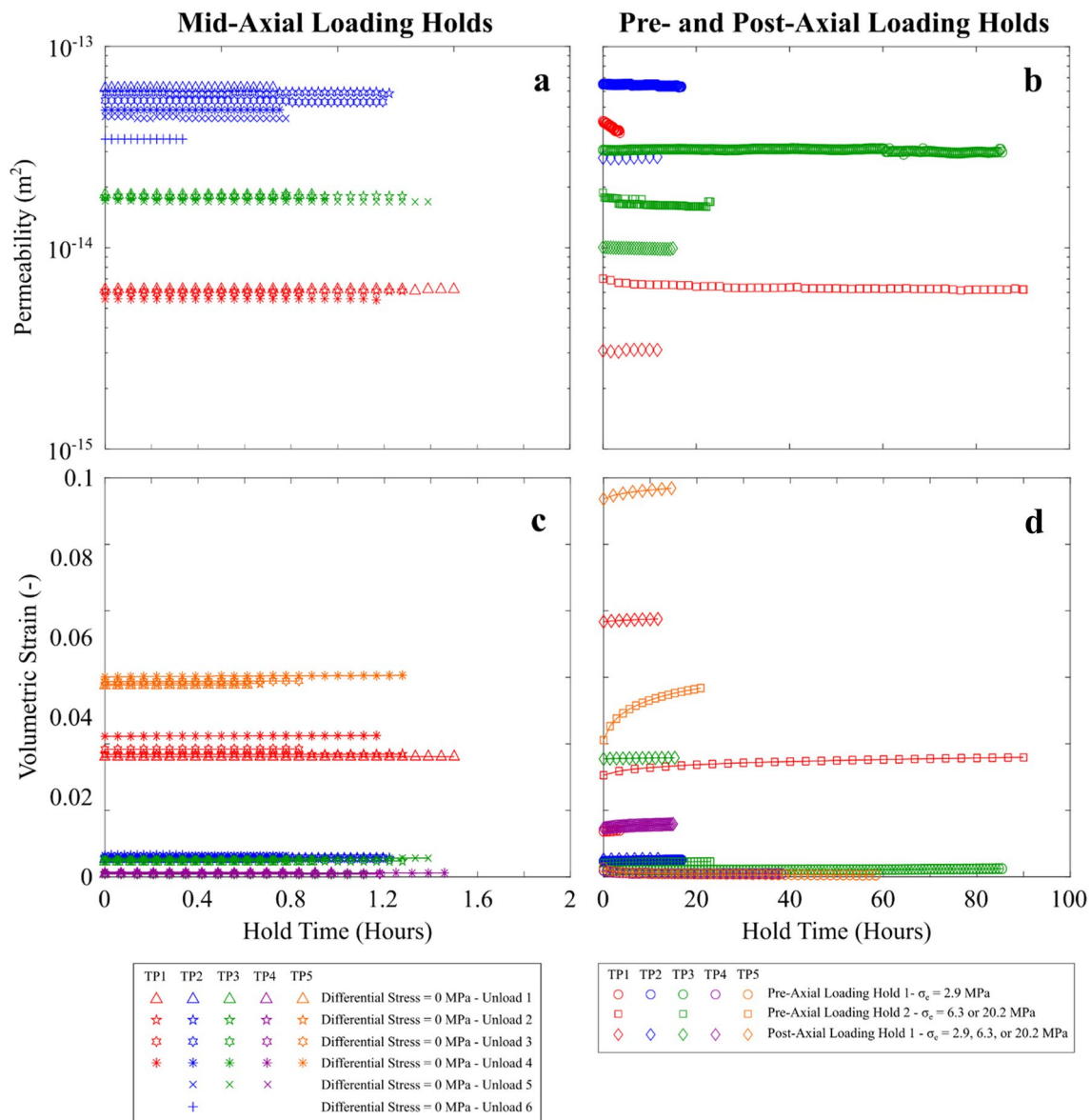
Fig. 10 Top row shows gas permeability measurements of TP1, TP2, and TP3 during the mid-axial loading holds (**a**) and pre/post-axial loading holds (**b**). The bottom row shows volumetric strain of all tests during the mid-axial loading hold (**c**) and pre/post-axial loading holds (**d**). All values shown are measured at hydrostatic stress conditions. See Fig. 6a for hold periods during testing

Bisnovat (2013) observed that the mechanical properties of the Ghareb declined precipitously with increasing water content, with property degradation peaking around 45% water content. Similarly, the water-weakening effect appears to be present during deformation of the tested Ghareb samples, which were fully water-saturated. Water-weakening is a well-known phenomenon where, for a given rock type and set of conditions, the interaction with water during deformation reduces rock strength and rigidity (Heap et al. 2009). Such weakening is well established to occur for chalks (Risnes et al. 2005; Cianta et al. 2015). In a carbonate rock, this occurs through three possible methods: (1)

if the rock is in an undrained state, often induced by rapid strain rates, the pore fluids can promote dilatancy hardening by temporarily reducing the effective pressure applied to the material due to the reduced hydraulic diffusivity (Rutter 1972); (2) concentration of stresses at calcite grain contacts can enhance dissolution that promotes pressure solution creep (Zhang et al. 2010; Gratier et al. 2013); 3) water can promote subcritical crack growth in calcite grains below the critical stress threshold (Bergsaker et al. 2016). Given that the relatively slow axial strain rates used ($\sim 10^{-5}$ s^{-1}) and that pore fluid pressure was externally controlled during the tests, the mechanical effect in (1) can be discounted.

Table 3 Quantitative properties determined from mechanical tests

Test Name	K	E	v	G
	GPa	GPa	–	GPa
HL1	2.0–18.1	–	–	–
HC1	0.4–11.3[a]	–	–	–
HC2	0.6–18.4[a]	–	–	–
TP1	1.35[b]	4.37	0.23	1.78
TP2	1.31[b]	4.31	0.15	1.89
TP3	1.22[b]	4.26	0.10	1.94
TP4	1.12[b]	2.87	0.13	1.28
TP5	1.34[b]	3.57	0.28	1.40

K bulk modulus, E Young's modulus, v Poisson's ratio, G shear modulus

[a]Moduli for hydrostatic creep tests were made using the slope of the loading rather than thorough unload-reload loops

[b]Bulk moduli for triaxial tests were made during loading rather than through unload-reload loops, using loading effective pressure from 1.5 to 3.5 MPa
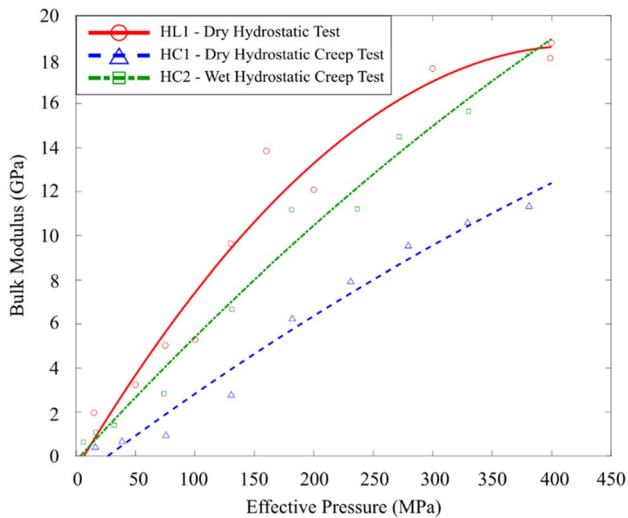

Fig. 11 Bulk moduli measured from unloading loops in dry hydrostatic test and loading during hydrostatic creep tests

This indicates the time-dependent deformation mechanisms of pressure solution creep (2) and subcritical crack growth (3) are likely the cause of the water-weakening observed in the Ghareb.

4.2 Time-Dependent Deformation at Hydrostatic Conditions

Time-dependent behavior is exhibited by materials which continue to deform without increasing the stress conditions (Costin 1987; Ti et al. 2009). Such behavior in rocks can be described as viscoelastic and/or visco-plastic, with the key difference being that viscoelastic behavior implies time-dependent deformation is recoverable when stress is reduced while visco-plastic behavior is characterized by non-recoverable, time-dependent deformation when stress is reduced. Time-dependent deformation in rocks occurs through mechanisms, such as subcritical crack growth and pressure solution creep, which necessitate rock-fluid interaction during deformation. Subcritical crack growth is generally attributed to stress corrosion, a process describing the chemical interaction of pore fluids preferentially at crack tips where stresses are concentrated in rocks (Atkinson 1984). Pressure solution creep conversely occurs through stress-driven dissolution at grain-grain contacts, followed by removal of the dissolved material either to precipitate in pore spaces or be removed by hydraulic diffusion from the rock system (Croizé et al. 2010; Gratier et al. 2013). Both mechanisms require rock-fluid interaction in order to occur, meaning that time-dependent behaviors depend on the material properties and fluid chemistry.

Carbonate rocks are well known for being strongly time-dependent (e.g., Rutter 1974; Brantut et al. 2014; Carpenter et al. 2016; Nicolas et al. 2017). Subcritical cracking has been demonstrated in calcite and carbonates in laboratory experiments conducted over short durations (Brantut et al. 2013; Violay et al. 2013; Bersgaker et al. 2016), but the dominant deformation mechanism for carbonate rocks over longer durations is pressure solution creep because of the dissolution kinetics of calcite (Plummer et al. 1979; Svensson and Dreybrodt 1992). The rate kinetics of calcite dissolution and precipitation enhance chemo-mechanical deformation processes, increasing viscoelastic behavior in calcite-rich rocks.

The time-dependency of the Ghareb can be clearly seen in Fig. 13, which compares the creep strain measured during the hydrostatic holds for the long-term creep experiments (Fig. 11a, b, c) and for the holds at hydrostatic conditions for the triaxial tests (Fig. 13d, e, f). The volumetric strains during each hold shown were normalized to show only the volumetric strain once pressure conditions were reached. The slope of the normalized strains curves indicates the instantaneous strain rate during each hold. Tables 4 and 5 show the volumetric strain rate and permeabilities of the HP and TP tests, during each hold shown in Fig. 13, as the samples were undergoing secondary stage creep (Brantut et al. 2013).

A few points are immediately clear from the creep strain data. First, the magnitude of the effective pressure directly affects the creep strain, and thus the strain rate. The greatest strain is universally exhibited, for both the long-term creep test and the triaxial test holds, when effective pressures are at their highest (~20 MPa). Conversely, when the stress is unloaded the greatest decrease in volumetric strain occurs when the pressures are at 5.62 MPa or lower. Second, both test types show some degree of time-dependency, there is

Fig. 12 **a** Young's modulus; **b** shear modulus; **c** Poisson's ratio. Symbols indicate averages, bars indicate ± 1 standard deviation. Dashed lines show linear trend with effective confining pressure
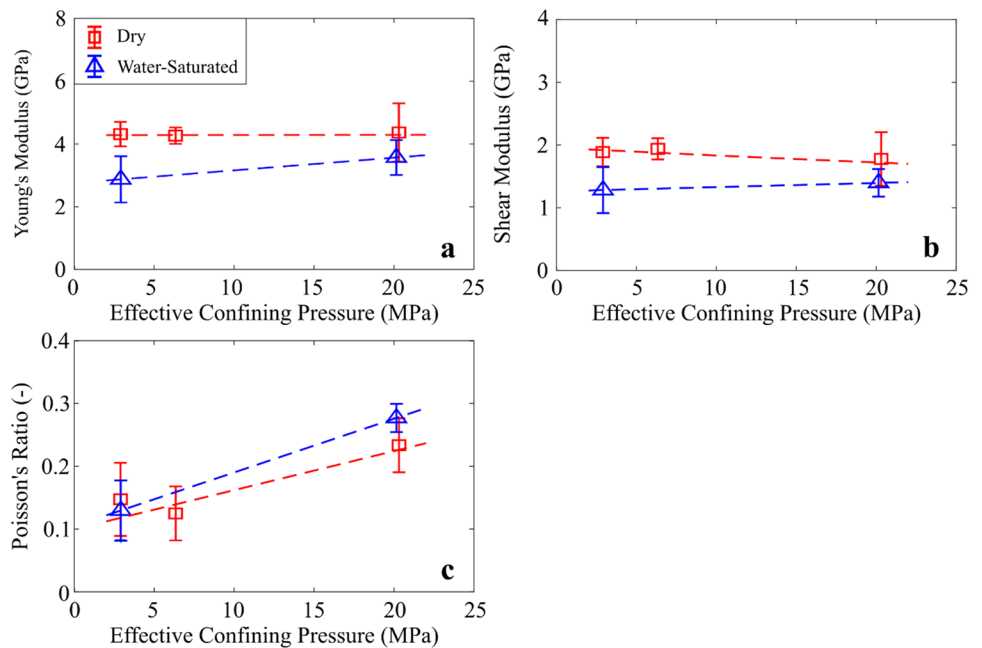
a stark difference between the creep observed between the dry triaxial test holds and the water-saturated tests. For the water-saturated tests, a large decrease in volumetric strain during holding is observed at the lowest pressures. At the same conditions in the dry test holds (TP1–TP3), pressurization to the lowest conditions (1–5 MPa) produces small but noticeable compaction during holding. Furthermore, at the highest pressures (~ 20 MPa) the dry tests exhibit less than half of the compaction observed by the water-saturated tests at the same conditions.

Taken together, time-dependency does appear to occur under dry conditions in the Ghareb samples, however, it is much more prominent when water is present. During the hydrostatic and triaxial tests, when pressure was reduced, strain did not return to previous levels, though there was some recovery when effective pressure was unloaded to below 10 MPa (Figs. 7b, 8a, b, 10c, d). Thus, deformation behavior of the Ghareb is primarily viscoplastic, with some viscoelastic behavior observed below ~ 10 MPa. Carbonate rocks exhibit ductile deformation mechanisms concurrent with brittle deformation mechanisms, such as plastic flow and crystal twinning (Croize et al. 2013), even at low pressures and temperatures. Such mechanisms may also introduce time-dependency regardless of the lack of pore fluids (Brantut et al. 2014; Nicolas et al. 2017).

4.3 Permeability Modification of Ghareb

While porosity and permeability are interrelated, they are not necessarily linearly related (Bernabé et al. 2003). From our data, it is reasonable to say that both porosity and permeability decrease with increased effective pressure (Tables 4,

5). However, reduction of effective pressure does not lead to a return to the previous permeability at that value. For the HP creep tests, the permeabilities at the lowest pressure during testing (~ 1 MPa) are reduced by 1–2 orders of magnitude between loading and unloading, depending on the sample. Likewise, the application of differential stress for TP1, TP2, and TP3 reduces the overall permeability to half of its previous average pre-axial loading (Table 5). Contrary to observations of permeability evolution increases observed when rocks deform by shear-enhanced dilation (Zhu and Wong 1997), as would be expected for TP2 and possibly TP3 (Fig. 7), brittle deformation and dilation did not enhance the post-test permeability. It appears that even if a rock exhibits dilant behavior characteristic of fracture formation, compaction through mechanical processes (e.g., grain rearrangement, grain crushing, etc.) in the Ghareb is sufficient to suppress the impact that fracture localization would have on enhancing permeability.

Overall, the permeability and volumetric strain is much lower for the HP tests than for the TP tests at similar effective pressures. It should be noted that the strains during the water-saturated TP tests are closer to the HP tests at similar effective pressures than the dry TP tests (Figs. 8b, e, h, 10d). This behavior could be due to a few factors: (1) the amount of time the HP tests are held at pressure is much greater than for the triaxial tests, allowing for more compaction and thus permeability reduction; (2) sample permeability measured during the triaxial tests was conducted on dry samples with air as the permeant, and gasses usually flow more easily through rock than fluids; (3) rock-fluid interaction is enhancing the volumetric strain rates relative to the dry tests, as is observed in Table 4. Although all
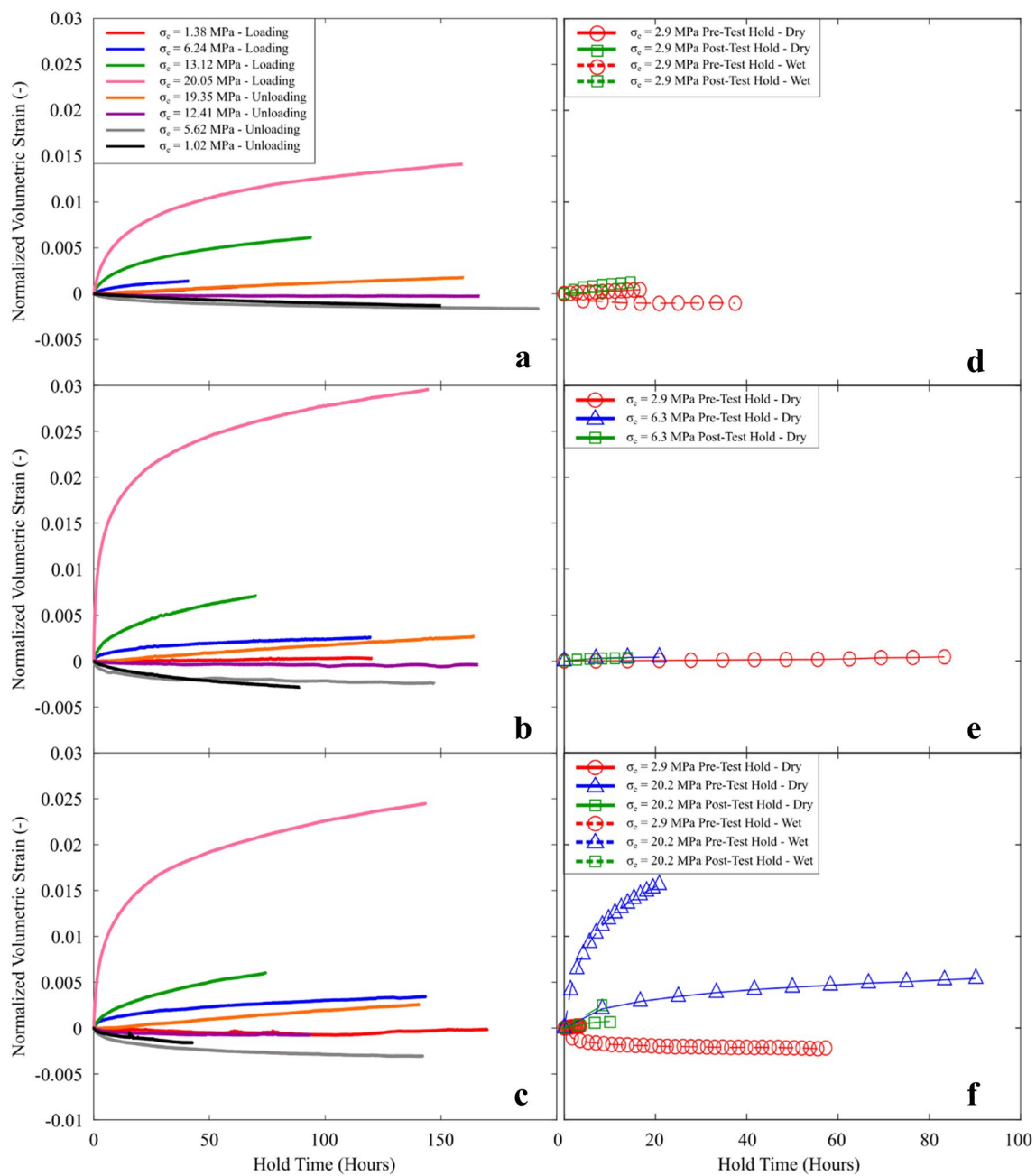
Fig. 13 Normalized volumetric strain during loading and unloading effective pressure holds for: **a** HP1; **b** HP2; **c** HP3; **d** TP2 and TP4; **e** TP3; **f** TP1 and TP5

three factors likely play a role, the effect of water is likely a significant contributor.

During the long-term creep tests, it was observed that the radial strains surpassed the axial strain when effective pressure was increased to 20.1 MPa (Fig. 8). During the triaxial tests at similar effective pressures, this behavior was not observed under the dry tests. However, similar behavior was observed in the water-saturated tests during the post-axial hold of TP5 (Table 5). Though permeability is not measured for TP4 and

TP5, the similarity between the observations and the HP test data is significant. Given Eq. (3), the rapid decrease in sample area relative to sample length means permeability will degrade less with continued creep strain. This anisotropic deformation is not expected under the isotropic stress state. However, the chemical reactions and direction of fluid flow may explain this behavior. Long-term water and acidic brine flow in carbonate rocks has been shown by others to occur as fluids follow the wider pore channels or fractures, increasing dissolution

Table 4 Volumetric strain rates ($\dot{\varepsilon}_v$) and permeabilities (k) for the hydrostatic creep permeability tests at different effective pressures during loading and unloading sections.

σ_{ep}	HP1		HP2		HP3	
	$\dot{\varepsilon}_v$	k	$\dot{\varepsilon}_v$	k	$\dot{\varepsilon}_v$	k
MPa	s^{-1}	m^2	s^{-1}	m^2	s^{-1}	m^2
1.4	$3.5*10^{-9}$	$3.7*10^{-16}$	$8.7*10^{-10}$	$1.3*10^{-15}$	$1.6*10^{-10}$	$1.3*10^{-15}$
6.2	$4.6*10^{-9}$	$2.1*10^{-17}$	$2.4*10^{-9}$	$1.7*10^{-16}$	$3.6*10^{-9}$	$3.1*10^{-16}$
13.1	$9.4*10^{-9}$	$5.9*10^{-18}$	$1.4*10^{-8}$	$1.9*10^{-16}$	$1.3*10^{-8}$	$2.0*10^{-16}$
20.1	$9.0*10^{-9}$	$4.3*10^{-18}$	$1.3*10^{-8}$	$1.3*10^{-16}$	$1.8*10^{-8}$	$1.2*10^{-16}$
12.4	$-6.0*10^{-11}$	$2.7*10^{-18}$	$-2.2*10^{-11}$	$1.1*10^{-16}$	$-4.4*10^{-10}$	$1.6*10^{-16}$
5.6	$-1.1*10^{-9}$	$1.5*10^{-18}$	$-9.8*10^{-10}$	$1.1*10^{-16}$	$-4.7*10^{-9}$	$1.6*10^{-16}$
1.0	$-1.5*10^{-9}$	$1.5*10^{-18}$	$-5.1*10^{-9}$	$1.6*10^{-16}$	$-6.4*10^{-9}$	$1.7*10^{-16}$

Values were interpreted when rocks were experiencing secondary creep

*Indicates the number is multiplied by the magnitude value presented

Table 5 Volumetric strain rates ($\dot{\varepsilon}_v$) and permeabilities (k) for the triaxial deformation tests pre- and post-axial loading at different effective pressures.

σ_{ep}	TP1		TP2		TP3		TP4		TP5	
	$\dot{\varepsilon}_v$	k	$\dot{\varepsilon}_v$	k	$\dot{\varepsilon}_v$	k	$\dot{\varepsilon}_v$	k	$\dot{\varepsilon}_v$	k
MPa	s^{-1}	m^2	s^{-1}	m^2	s^{-1}	m^2	s^{-1}	m^2	s^{-1}	m^2
2.9 (Pre-Axial)	$2.2*10^{-8}$	$4.0*10^{-14}$	$3.7*10^{-9}$	$6.4*10^{-14}$	$2.9*10^{-9}$	$3.1*10^{-14}$	$-3.1*10^{-9}$		$-9.3*10^{-10}$	
2.9 (Post-Axial)			$4.5*10^{-9}$	$2.8*10^{-14}$			$1.4*10^{-8}$			
6.3 (Pre-Axial)					$3.8*10^{-9}$	$1.6*10^{-14}$				
6.3 (Post-Axial)					$3.6*10^{-9}$	$9.9*10^{-15}$				
20.2 (Pre-Axial)	$7.0*10^{-9}$	$6.3*10^{-15}$							$1.1*10^{-7}$	
20.2 (Post-Axial)	$1.3*10^{-8}$	$3.1*10^{-15}$							$3.5*10^{-8}$	

*Indicates the number is multiplied by the magnitude value presented

through these preferential flow paths which lead to the formation of localized channel paths (Xie et al. 2011; Bauer et al. 2013; Madland et al. 2006; Khather et al. 2022). This process requires long-term fluid flow in order for sufficient linkage of dissolution channels to occur (Khather et al. 2022). As fluid flow in our samples is parallel to the sample length and perpendicular to the sample radius, water may be preferentially dissolving pathways parallel to the sample length. These pathways in our samples would be perpendicular to the lateral direction, and thus more of their closure during loading would be accounted for by the lateral strain. This suggests hydrological and chemical processes are coupled with mechanical processes and control deformation when the Ghareb is water-saturated, especially above certain effective pressure conditions. However, microscopic analysis of these samples was not conducted so the exact mechanism is uncertain.

4.4 Implications for Potential Nuclear Waste Disposal in Ghareb

Our results indicate the Ghareb is a soft, weak rock that exhibits significant elasto-viscoplastic behavior under short- and long-time scales. This has implications for the stability of the borehole during development and operation of the reservoir. At the expected depth for disposal, the initial effective pressure of the formation is expected to be ~8 MPa prior to repository setup, and not to exceed 20 MPa during operation of the repository, with a near hydrostatic in situ stress state (Bisnovat et al. 2015). Given the $P*$ value determined, this suggests that the introduction of more than 4–7 MPa effective mean stress to the formation is liable to induce irreversible compaction. The Ghareb is expected to only be partially water-saturated (i.e., 1–25%) at the target depth, so the effect of water-weakening is not expected to as great as what is seen here (Bisnovat 2013). However, our observations show non-trivial viscoplastic creep occurs even under dry conditions, indicating that creep deformation will still be expected around the vicinity of the borehole even with low fluid content. The introduction of fluids during drilling, as well as compaction-induced pore pressurization, may enhance deformation in the near-wellbore vicinity over large time scales.

The permeability of the formation is comparable to other chalk formations (Hamouda et al. 2008; Alam et al. 2015), though is lower than many chalk reservoirs known from hydrocarbon recovery. Increasing stress appears to reduce

permeability overall whether the rock is deformed under brittle or more ductile pressures conditions (Table 4). This suggests that, even if fracturing occurs in the vicinity of the borehole during drilling and emplacement, compaction and creep in the surrounding Ghareb formation is likely to negate any permeability changes due to the opening of preferential pathways. The hydrological conditions, particularly fluid flow direction, seem to exert control over deformation of the Ghareb over short-time scales at higher pressures (Fig. 8). Preferential dissolution of the Ghareb may occur along the primary flow direction, generating anisotropy of deformation in the reservoir. This may be of particular importance along any bedding planes or pre-existing fault planes in the Ghareb, which are strong pathways for fluid flow in sedimentary rocks (Caine et al. 1996; Bjørlykke and Høeg 1997; Manzocchi et al. 2010). Such fluid flow may produce greater compaction perpendicular to these planes, which could lead to significant consequences, such as reservoir compaction, induced seismicity, and borehole deformation, which may inhibit repository operation.

The hydrological, mechanical, and chemical processes that deform the Ghareb are strongly coupled, meaning that even minor alterations to the in situ conditions will impact how the host rock deforms during repository operation. Additionally, as the repository expands to many boreholes, interaction between the many zones of deformation is likely to further exacerbate hydromechanical deformation. Further modeling of the coupled hydro-chemo-mechanical deformation processes is needed to understand the level of risk over the long-time scales required to isolate the radioactive materials. The key to this issue is better understanding of the different micromechanisms that produce viscoelastic deformation of the Ghareb and the expected in situ changes during repository operation, as such altered conditions, such as the introduction of fluids or temperature, will alter mechanisms controlling deformation and thus behavior of the Ghareb. Temperature is also strongly coupled with the other processes operating in situ, for example increasing temperature may mechanically weaken the rock, increase the flow rate of fluids, and accelerate chemical reactions and diffusivity. Further work in future is needed to characterize the thermal impact of nuclear waste disposal on the Ghareb before repository operation can begin.

5 Conclusions

We conducted a series of hydromechanical experiments to measure the different properties of the Ghareb and how the coupling of the various deformation processes altered rock behavior. The chalk was shown to be mechanically weak, with correspondingly low mechanical parameters and rock failure only occurring at very low effective pressures. The water-saturated samples exhibited strong water-weakening during deformation when compared to the dry tests at similar conditions, as water saturation appears to enhance compaction or inhibit dilatancy during deformation. Significant time-dependent or viscoelastic behavior was observed during the hydrostatic creep tests and triaxial tests under isotropic stress conditions. This time-dependent behavior is strongly pressure controlled and occurred under both dry and water-saturated test conditions during hold periods, indicating ductile deformation mechanisms are occurring during both tests even at room temperature which compete with chemomechanical deformation, such as subcritical cracking and pressure solution, under water-saturated conditions. Fluids appear to also promote deformation anisotropy in the Ghareb when the samples are pressurized near-to or above the grain crushing pressure $P*$ for the rocks. The results strongly suggest: (1) minor fluctuations in the in situ hydrological and mechanical conditions are likely to alter deformation behavior of the Ghareb especially in the near-wellbore vicinity; (2) the various hydro-chemo-mechanical processes are strongly coupled during deformation, such that predicting long-term deformation requires an understanding of all these parameters and their coupling; and (3) the expected in situ changes induced by setup and operation of the repository must be well quantified for large time scales as each parameter affects how the rock will respond to the other in situ conditions. Future research and modeling should expand upon this work by examining how the different mechanisms of deformation are affected by changes to in situ conditions, particularly the effect of thermal loading from emplaced waste on the host rock.

Declarations

Conflict of interest The authors report no conflicts of interest exist in this study.

References

Agosta F, Alessandroni M, Antonellini M, Tondi E, Giorgioni M (2010) From fractures to flow: A field-based quantitative analysis of an outcropping carbonate reservoir. Tectonophysics 490(3–4):197–213

Alam AB, Fujii Y, Fukuda D, Kodama JI, Kaneko K (2015) Fractured rock permeability as a function of temperature and confining pressure. Pure Appl Geophys 172:2871–2889

Ali S (2011) Nuclear Waste Disposal Methods. Standford University. https://large.stanford.edu/courses/2011/ph241/ali2/ (Page consultée le 21 octobre 2012)

Amour F, Christensen HF, Hajiabadi MR, Nick HM (2021) Effects of porosity and water saturation on the yield surface of Upper Cretaceous reservoir chalks from the Danish North Sea. J Geophys Res Solid Earth126(3):p.e2020JB020608

An Z, Di Q, Wang R, Wang M (2013) Multi-geophysical investigation of geological structures in a pre-selected high-level radioactive waste disposal area in northwestern China. J Environ Eng Geophys 18(2):137–146

ASTM (2001) Standard Practices for Preparing Rock Core Specimens and Determining Dimensional and Shape Tolerances. Annual Book of ASTM Standards

Atkinson BK (1984) Subcritical crack growth in geological materials. J Geophys Res 89(B6):4077–4114

Bauer A, Walle LE, Stenebråten J, Papamichos E (2013) Impact of acidizing-induced wormholes in chalk on rock strength. In47th US Rock Mechanics/Geomechanics Symposium. OnePetro

Bergsaker AS, Røyne A, Ougier-Simonin A, Aubry J, Renard F (2016) The effect of fluid composition, salinity, and acidity on subcritical crack growth in calcite crystals. J Geophys Res 121(3):1631–1651

Bernabé Y, Mok U, Evans B (2003) Permeability-porosity relationships in rocks subjected to various evolution processes. Pure Appl Geophys 160:937–960

Beswick AJ, Gibb FG, Travis KP (2014) Deep borehole disposal of nuclear waste: engineering challenges. Proc Inst Civil Eng Energy 167(2):47–66

Bisnovat K (2013) Mechanical and petrophysical behavior of oil shale from the Judea Plains, Israel. Ben-Gurion University of the Negev, Faculty of Natural Sciences, Department of Geological and Environmental Sciences

Bisnovat K, Hatzor YH, Vinegar HJ, Nguyen SV, Palchik V, Feinstein S (2015) Mechanical and petrophysical behavior of organic-rich chalk from the Judea Plains, Israel. Mar Pet Geol 64:152–164

Bjørlykke K, Høeg K (1997) Effects of burial diagenesis on stresses, compaction and fluid flow in sedimentary basins. Mar Pet Geol 14(3):267–276

Brady PV, Arnold BW, Freeze GA, Swift PN, Bauer SJ, Kanney JL, Rechard RP, Stein JS (2009) Deep borehole disposal of high-level radioactive waste. Sandia Report SAND2009-4401, Sandia National Laboratories, Albuquerque, New Mexico

Brady PV, Arnold BW, Altman SJ, Vaughn, P (2012) Deep borehole disposal of nuclear waste summary (No. SAND2012-7789). Sandia National Laboratories (SNL), Albuquerque, NM, and Livermore, CA (United States)

Brantut N, Heap MJ, Meredith PG, Baud P (2013) Time-dependent cracking and brittle creep in crustal rocks: a review. J Struct Geol 52:17–43

Brantut N, Heap MJ, Baud P, Meredith PG (2014) Mechanisms of time-dependent deformation in porous limestone. J Geophys Res 119(7):5444–5463

Brantut N, Baker M, Hansen LN, Baud P (2018) Microstructural control of physical properties during deformation of porous limestone. J Geophys Res 123(6):4751–4764

Caine JS, Evans JP, Forster CB (1996) Fault zone architecture and permeability structure. Geology 24(11):1025–1028

Carpenter BM, Ikari MJ, Marone C (2016) Laboratory observations of time-dependent frictional strengthening and stress relaxation in natural and synthetic fault gouges. J Geophys Res 121(2):1183–1201

Chapman N, Hooper A (2012) The disposal of radioactive wastes underground. Proc Geol Assoc 123(1):46–63

Cherry JA, Alley WM, Parker BL (2014) Geologic disposal of spent nuclear fuel. Bridge Emerg Issues Earth Resour Eng 44(1):51–59

Choens RC, Bauer SJ, Shalev E, Lyakhovsky V (2021) Modelling yield cap evolution in sandstone based on brittle creep experiments. Int J Rock Mech Min Sci 141:104706

Ciantia MO, Castellanza R, Di Prisco C (2015) Experimental study on the water-induced weakening of calcarenites. Rock Mech Rock Eng 48(2):441–461

Costin LS (1987) Time-dependent deformation and failure. Fract Mech Rock 167:215

Croizé D, Renard F, Bjørlykke K, Dysthe DK (2010) Experimental calcite dissolution under stress: evolution of grain contact microstructure during pressure solution creep. J Geophys Res. https://doi.org/10.1029/2010JB000869

Croize D, Renard F, Gratier JP (2013) Compaction and porosity reduction in carbonates: A review of observations, theory, and experiments. Adv geophys 54:181–238

Dangelmayr MA, Bussod GY, Reimus PW, WoldeGabriel G, Calvo R, Harris RJ et al (2022) Uranium retardation capacity of Lithologies from the Negev Desert, Israel—rock characterization and Sorption experiments. Minerals 12(6):728

David C, Wong TF, Zhu W, Zhang J (1994) Laboratory measurement of compaction-induced permeability change in porous rocks: Implications for the generation and maintenance of pore pressure excess in the crust. Pure Appl Geophys 143(1):425–456

David C, Menendez B, Zhu W, Wong TF (2001) Mechanical compaction, microstructures and permeability evolution in sandstones. Phys Chem Earth Part A 26(1–2):45–51

Delay J, Lebon P, Rebours H (2010) Meuse/Haute-Marne centre: next steps towards a deep disposal facility. J Rock Mech Geotech Eng 2(1):52–70

Faybishenko B, Birkholzer J, Sassani D, Swift P (2017) International Approaches for Nuclear Waste Disposal in Geological Formations: Geological Challenges in Radioactive Waste Isolation—Fifth Worldwide Review. United States. https://doi.org/10.2172/1353043

Fortin J, Stanchits S, Dresen G, Gueguen Y (2009) Acoustic emissions monitoring during inelastic deformation of porous sandstone: comparison of three modes of deformation. Pure Appl Geophys 166(5):823–841

Freeze GA, Leigh CD, Sevougian SD, Gross M (2012) A safety framework for disposal of heat-generating waste in salt: annotated outline (No. SAND2012-10797P). Sandia National Lab. (SNL-NM), Albuquerque, NM (United States)

Gratier JP, Dysthe DK, Renard F (2013) The role of pressure solution creep in the ductility of the Earth's upper crust. Adv Geophys 54:47–179

Hamouda AA, Karoussi O, Chukwudeme EA (2008) Relative permeability as a function of temperature, initial water saturation and

flooding fluid compositions for modified oil-wet chalk. J Petrol Sci Eng 63(1–4):61–72

Heap MJ, Baud P, Meredith PG, Bell AF, Main IG (2009) Time-dependent brittle creep in Darley Dale sandstone. J Geophys Res. https://doi.org/10.1029/2008JB006212

Jove-Colon C, Ho T, Coker E, Lopez C, Sanchez A, Kuhlman K, Mills M, Kruichak K, Matteo E (2022) International Collaborations Activities on Disposal in Argillite R&D: Characterization Studies and Modeling Investigations (No. SAND2022-10733R). Sandia National Lab.(SNL-NM), Albuquerque, NM (United States); Sandia National Laboratories,, Carlsbad, NM

Kallesten EI, Cherif Y, Madland MV, Korsnes RI, Omdal E, Andersen PØ, Zimmermann U (2021) Validation study of water weakening research from outcrop chalks performed on Eldfisk reservoir cores. J Petrol Sci Eng 198:108164

Khather M, Saeedi A, Myers MB, Giwelli A, Esteban L (2022) Impacts of limestone vertical permeability heterogeneity on fluid-rock interaction during CCS. Transport Porous Media. https://doi.org/10.1007/s11242-022-01751-1

Kim JS, Kwon SK, Sanchez M, Cho GC (2011) Geological storage of high level nuclear waste. KSCE J Civ Eng 15(4):721–737

Klein E, Baud P, Reuschlé T, Wong TF (2001) Mechanical behaviour and failure mode of Bentheim sandstone under triaxial compression. Phys Chem Earth Part A 26(1–2):21–25

Klinkenberg LJ (1941) The permeability of porous media to liquids and gases. Am Petrol Inst Drilling Prod Pract 2:200–213

Koopmans MP, Rijpstra WIC, de Leeuw JW, Lewan MD, Damsté JSS (1998) Artificial maturation of an immature sulfur-and organic matter-rich limestone from the Ghareb Formation, Jordan. Org Geochem 28(7–8):503–521

Kuhlman KL (2017) WIPP: From URL to disposal Facility (No. SAND2017-6250PE). Sandia National Lab.(SNL-NM), Albuquerque, NM (United States)

Laverov NP, Yudintsev SV, Kochkin BT, Malkovsky VI (2016) The Russian strategy of using crystalline rock as a repository for nuclear waste. Elements 12(4):253–256

Madland MV, Finsnes A, Alkafadgi A, Risnes R, Austad T (2006) The influence of CO2 gas and carbonate water on the mechanical stability of chalk. J Petrol Sci Eng 51(3–4):149–168

Manzocchi T, Childs C, Walsh JJ (2010) Faults and fault properties in hydrocarbon flow models. Geofluids 10(1–2):94–113

Martin CD (1997) Seventeenth Canadian geotechnical colloquium: the effect of cohesion loss and stress path on brittle rock strength. Can Geotech J 34(5):698–725

McBeck J, Ben-Zion Y, Renard F (2022) Volumetric and shear strain localization throughout triaxial compression experiments on rocks. Tectonophysics 822:229181

Nicolas A, Fortin J, Regnet JB, Verberne BA, Plümper O, Dimanov A, Spiers CJ, Guéguen Y (2017) Brittle and semibrittle creep of Tavel limestone deformed at room temperature. J Geophys Res 122(6):4436–4459

Plummer LN, Parkhurst DL, Wigley TML (1979) Critical review of the kinetics of calcite dissolution and precipitation. American Chemical Society, Washington, D.C.

Ramana MV (2018) Technical and social problems of nuclear waste. Wiley Interdiscip Rev 7(4):e289

Risnes R, Madland MV, Hole M, Kwabiah NK (2005) Water weakening of chalk—mechanical effects of water–glycol mixtures. J Petrol Sci Eng 48(1–2):21–36

Ruddy I, Andersen MA, Pattillo PD, Bishlawi M, Foged N (1989) Rock compressibility, compaction, and subsidence in a high-porosity chalk reservoir: a case study of Valhall field. J Petrol Technol 41(07):741–746

Rudnicki JW (2004) Shear and compaction band formation on an elliptic yield cap. J Geophys Res. https://doi.org/10.1029/2003JB002633

Rutqvist J (2014) Fractured rock stress-permeability relationships from in situ data and effects of temperature and chemical-mechanical couplings. Geofluids 15(1–2):48–66

Rutter EH (1974) The influence of temperature, strain rate and interstitial water in the experimental deformation of calcite rocks. Tectonophysics 22(3–4):311–334

Sasaki T, Rutqvist J (2022) Effects of time-dependent deformation of shale on the integrity of a geological nuclear waste repository. Int J Rock Mech Min Sci 158:105206

Schutjens PMTM, Hanssen TH, Hettema MHH, Merour J, De Bree P, Coremans JWA, Helliesen G (2004) Compaction-induced porosity/permeability reduction in sandstone reservoirs: data and model for elasticity-dominated deformation. SPE Reserv Eval Eng 7(03):202–216

Shitrit O, Hatzor YH, Feinstein S, Palchik V, Vinegar HJ (2016) Effect of kerogen on rock physics of immature organic-rich chalks. Mar Pet Geol 73:392–404

Shitrit O, Hatzor YH, Feinstein S, Vinegar HJ (2017) Acoustic and petrophysical evolution of organic-rich chalk following maturation induced by unconfined pyrolysis. Rock Mech Rock Eng 50(12):3273–3291

Siren T, Hakala M, Valli J, Kantia P, Hudson JA, Johansson E (2015) In situ strength and failure mechanisms of migmatitic gneiss and pegmatitic granite at the nuclear waste disposal site in Olkiluoto, Western Finland. Int J Rock Mech Min Sci 79:135–148

Svensson U, Dreybrodt W (1992) Dissolution kinetics of natural calcite minerals in CO_2-water systems approaching calcite equilibrium. Chem Geol 100(1–2):129–145

Teufel LW, Rhett DW, Farrell HE (1991) Effect of reservoir depletion and pore pressure drawdown on in situ stress and deformation in the Ekofisk field, North Sea. In The 32nd US Symposium on Rock Mechanics (USRMS). OnePetro

Ti KS, Huat BB, Noorzaei J, Jaafar MS, Sew GS (2009) A review of basic soil constitutive models for geotechnical application. Electron J Geotech Eng 14:1–18

Tsang CF, Barnichon JD, Birkholzer J, Li XL, Liu HH, Sillen X (2012) Coupled thermo-hydro-mechanical processes in the near field of a high-level radioactive waste repository in clay formations. Int J Rock Mech Min Sci 49:31–44

Vajdova V, Baud P, Wong TF (2004) Compaction, dilatancy, and failure in porous carbonate rocks. J Geophys Res. https://doi.org/10.1029/2003JB002508

Violay M, Nielsen S, Spagnuolo E, Cinti D, Di Toro G, Di Stefano G (2013) Pore fluid in experimental calcite-bearing faults: abrupt weakening and geochemical signature of co-seismic processes. Earth Planet Sci Lett 361:74–84

Wong TF, Baud P (1999) Mechanical compaction of porous sandstone. Oil Gas Sci Technol 54(6):715–727

Wong TF, Baud P, Klein E (2001) Localized failure modes in a compactant porous rock. Geophys Res Lett 28(13):2521–2524

Xie SY, Shao JF, Xu WY (2011) Influences of chemical degradation on mechanical behaviour of a limestone. Int J Rock Mech Min Sci 48(5):741–747

Zhang J, Wong TF, Davis DM (1990) Micromechanics of pressure-induced grain crushing in porous rocks. J Geophys Res 95(B1):341–352

Zhang X, Spiers CJ, Peach CJ (2010) Compaction creep of wet granular calcite by pressure solution at 28 C to 150 C. J Geophys Res. https://doi.org/10.1029/2008JB005853

Zhu W, Wong TF (1997) The transition from brittle faulting to cataclastic flow: Permeability evolution. J Geophys Res 102(B2):3027–3041